PHYSICAL REVIEW B VOLUME 12, NUMBER 8 15 OCTOBER 1975

Electronic structure of disordered CuNi alloys

A. Bansil and L. Schwartz*
Department of Physics, Brandeis University, Waltham, Massachusetts 02154

H. Ehrenreich†
Division of Engineering and Applied Physics, Harvard University, Cambridge, Massachusetts 02138
(Received 10 June 1975)

We present the complex energy bands and electronic densities of states in paramagnetic CuNi alloys. The calculations are based on the use of muffin-tin potentials within the framework of the average-t-matrix approximation. The theory is shown to predict reasonably the electronic spectrum over a wide range of energies and alloy compositions. The experiments to be discussed include photoemission measurements of the density of states and Dingle-temperature measurements of the damping of both the neck and belly orbits. The half-width of the Ni virtual bound state in Cu-rich CuNi alloys is discussed in detail.

I. INTRODUCTION

In recent years there has been renewed interest in the study of the electronic properties of substitutional alloys. Because such systems lack the translational symmetry of ordered crystals, their eigenstates cannot be characterized in terms of the energy-band picture usually associated with Bloch's theorem. Substantial progress, however, has been made by the application of multiple-scattering techniques[1-3] utilizing single-site or mean-field approximations. The essential feature of this approach is that the individual atoms are viewed as being embedded in a periodic effective medium whose choice is open and can be made either self-consistently or non-self-consistently. These two choices lead, respectively, to the coherent-potential[4,5] (CPA) and average-t-matrix (ATA) approximations.[6,7] While the ATA correctly describes the qualitative features of the alloy spectrum, the CPA is known to be the more accurate of the two approximations.

Much of the work on the alloy problem in past years has been concerned with properties of simple one- and two-band tight-binding model Hamiltonians.[8-11] Lately, however, multiple-scattering techniques have been applied to more realistic alloy Hamiltonians and, in particular, to the muffin-tin model.[12-17] Such calculations are of importance because the tight-binding models are not suited to describing measured Fermi-surface and optical properties. The muffin-tin model is also attractive from a theoretical viewpoint because it allows the numerical methods relevant to Korringa, Kohn, and Rostoker (KKR) and augmented-plane-wave (APW) calculations[18] in ordered solids to be brought to bear on the alloy problem.

The formalism required for the application of the ATA and CPA to the muffin-tin model has been discussed by several authors.[15-17] Due to the complicated numerical calculations required for the self-consistent solution of the CPA equations, this approach has not yet been implemented. By contrast, calculations based on a muffin-tin ATA scheme are only slightly more difficult than conventional energy-band computations. In a recent publication we have shown that average-t-matrix calculations lead to a reasonable description of α-phase CuZn alloys.[13] It was argued in Ref. 13, that the spectrum of the alloy could be characterized in terms of complex energy bands. (The real and imaginary parts of the complex bands correspond, respectively, to the quasiparticle energies and lifetimes.) This approach has the advantage that the calculation of the complex energy bands is a relatively straightforward matter, the central equations being directly related to the KKR equations of band theory. Nevertheless, it should be emphasized that in contrast to the real crystalline band structure, the complex energy bands do not, by themselves, contain enough information for the calculation of the average electronic density of states.

While the results reported in Ref. 13 are encouraging, we note that CuZn is a relatively simple system in the sense that the constituent d bands (being separated by ~0.5 Ry) are essentially independent. A more important test of the ATA muffin-tin scheme is provided by the paramagnetic CuNi system because in this case, the two d bands interact appreciably and are both expected to hybridize with the conduction bands.

In the present paper we consider the complex energy bands and density of states in CuNi alloys.[19] That computations of the electronic density of states are now feasible is due to two developments since our earlier work on the CuZn system. First, Schwartz and Bansil[15] have derived equations for the ATA spectral density $a(\vec{k}, E)$. Once this quantity is known, the average density of states $\langle\rho(E)\rangle$ is obtained by integration over all vectors $\vec{k}$ in the first Brillouin zone. Second, it was Bansil's[20] development of the *special directions* method that made tractable the evaluation of these potentially difficult Brillouin-zone integrations. Calculations over a wide range of energies and alloy compositions are now practical, and we have studied in detail the structure of the complex energy bands, the spectral densities, and the average density of states.

In addition to the average density of states, the results presented in Ref. 15 can, in principle, be used to compute the separate contributions of the two components to the alloy spectrum. It turns out, however, that in CuNi alloys, where the constituent d bands interact strongly, the ATA expressions for the component densities of states are unreliable. In particular, these quantities may become negative in the energy range between the Cu and Ni $3d$ resonances. It is, of course, possible that in other systems, less complicated than CuNi, the ATA may provide an adequate picture of the component state densities. Nevertheless, it seems clear that the ATA does not describe these more detailed properties of the alloy as well as it does the average total spectrum.

A summary of the muffin-tin ATA formalism is given in Sec. II. The relevant numerical techniques are discussed in an Appendix. Since charge-transfer and lattice-expansion effects are believed to be negligible in CuNi alloys,[21] the renormalized-atom method[22] can be used directly to construct neutral muffin-tin potentials for the two atomic constituents. By contrast, in the case of α-CuZn alloys, the renormalized-atom potentials must be adjusted to take account of both charge transfer and lattice dilation.[13]

The complex energy bands are considered in Sec. III A. In the present case, even though we have ten d bands intersecting the common conduction band, the classification of the quasiparticle states is found to be surprisingly simple. The real and imaginary parts of the complex bands are shown to represent quantitatively the location and widths of the corresponding peaks in the spectral density function. This further justifies the use of complex bands to represent the quasiparticle states of the alloy. Section III B presents the densities of states for the entire range of alloy compositions. The characteristic features of the alloy densities of states are discussed in relation to the complex bands. In particular, we consider the behavior of the Ni virtual bound state[23] and the structure in the Cu subband. The present results are also compared with the predictions of the most recent tight-binding model Hamiltonian calculations.[9]

The predictions of the theory are compared with a variety of experimental results in Sec. IV. Good agreement is found with both low-energy and x-ray photoemission (XPS) measurements of the densities of states.[24-27] The predicted half-width of the Ni virtual bound state is in good agreement with the available experimental data for Ni concentrations between 10 and 30 %. For Ni concentrations below 5%, however, the calculated value of the half-width is twice as large as that deduced by Drew and Doezema[28] from optical-absorption measurements. (It should be noted that the tight-binding model Hamiltonian calculations of Ref. 9 predict a vanishing virtual-bound-state half-width in the limit of zero Ni concentration.) Finally, we compare our results for the Fermi-surface properties of the Cu-rich alloys with de Haas–van Alphen[29,30] and positron-annihilation measurements.[31] The predicted changes in the neck radius of Cu with Ni concentration are quite different from the rigid-band model[32] but in substantial agreement with experiment. The calculated Dingle temperatures for both the neck and the belly orbits are in good agreement with those obtained in the most recent experiments.[30]

The present results, taken together with our earlier results on α-CuZn and the recent calculations[33,34] on transition-metal hydrides suggest that the muffin-tin ATA is capable of describing the average electronic properties of a wide variety of disordered alloys. In view of this, a further study of other alloy systems within the present framework and extensions to the CPA appear to be warranted.

II. FORMULATION OF THE PROBLEM

A. Formalism

We consider a muffin-tin model of the substitutional binary alloy.[35] In this model the disordered potential can be expressed as a sum of nonoverlapping spherically symmetric contributions. The potential is then finite within a muffin-tin sphere of radius r_m surrounding each of the lattice sites $\{\vec{R}_n\}$ and is constant (by convention, zero) in the region between the spheres. The single-particle Hamiltonian may be written

$$H = p^2/2m + \sum_n v_n^{A(B)}(\vec{r}) \ . \qquad (2.1)$$

Within the muffin-tin spheres (i.e., $|\vec{r} - \vec{R}_n| < r_m$), the value of

$$v_n^{A(B)}(\vec{r}) \equiv v^{A(B)}(|\vec{r} - \vec{R}_n|) \qquad (2.2)$$

depends only on whether an A or B atom occupies the site n. The arrangement of the A and B atoms throughout the lattice is assumed to be random; their relative concentrations are x and $y \equiv 1 - x$.

The fact that the atomic potentials are spherically symmetric implies that the muffin-tin model is most easily described in terms of an angular-momentum representation. In this approach the properties of the point lattice and the atomic constituents are conveniently separated. The crystal lattice enters through the energy- and momentum-dependent matrix

$$B_{LL'}(\vec{k}, E) = [\, j_l(\kappa r) j_{l'}(\kappa r')]^{-1} \sum_{\vec{R}_n \neq \vec{0}} \int e^{i\vec{k}\cdot\vec{R}_n} \times G_0(\vec{r} - \vec{r}\,' - \vec{R}_n) Y_L(\vec{r}) Y_{L'}(\vec{r}\,') \, d\Omega_{\vec{r}} \, d\Omega_{\vec{r}\,'} \; . \tag{2.3}$$

Here $L \equiv (l, m)$, $\kappa = E^{1/2}$, $j_l(x)$ is the spherical Bessel function, $Y_L(\vec{x})$ denotes a real spherical harmonic of the angles associated with the vector $\vec{x}$, and

$$G_0(\vec{r}) = -e^{i\kappa r}/4\pi r \tag{2.4}$$

is the usual free-electron Green's function. [$B_{LL'}(\vec{k}, E)$ is independent of r and r', provided both r and $r' < r_m$.] The properties of the $A(B)$ potentials are represented by the energy shell matrix elements, $\tau_l^{A(B)}(E)$ of the atomic scattering operators. These quantities can, in turn, be expressed in terms of the more familiar atomic phase shifts $\delta_l^{A(B)}(E)$

$$\tau_l^{A(B)}(E) = -\kappa^{-1} e^{i\delta_l^{A(B)}} \sin\delta_l^{A(B)} \; . \tag{2.5}$$

In the case of a perfect crystal, the utility of the angular-momentum representation is illustrated by the KKR equation[18] of band theory,

$$\| \tau^{-1}(E) - B(\vec{k}, E) \| = 0 \; . \tag{2.6}$$

For a given $\vec{k}$ in the first Brillouin zone, the solution of this equation determines a sequence of eigenvalues $E_n(\vec{k})$. In practice, the size of the determinant in (2.6) is limited by the fact that the phase shifts for $l \geq 3$ are negligible for many noble and transition metals.

In the average-t-matrix approximation (ATA), the electronic properties of the alloy are described in terms of a periodic effective lattice of complex muffin-tin potentials. The individual effective potentials are so chosen as to reproduce the average scattering at each lattice site,

$$\tau_l^{\mathrm{eff}}(E) = x\tau_l^A(E) + y\tau_l^B(E) \equiv \langle \tau_l(E) \rangle \; . \tag{2.7}$$

Within this framework, Schwartz and Bansil[15] have shown that the average electronic density of states (per site and per spin) is given by

$$\langle \rho(E) \rangle = N^{-1} \sum_{\vec{k}} a(\vec{k}, E) \; , \tag{2.8a}$$

where

$$a(\vec{k}, E) = a_0(\vec{k}, E) + \pi^{-1} \,\mathrm{Im}\,\mathrm{Tr} \left\{ T(\vec{k}, E) \left[\langle \tau(E) \rangle^{-1} \left(x \frac{d}{dE} \ln[\tau^A(E)] + y \frac{d}{dE} \ln[\tau^B(E)] \right) + \frac{dB(\vec{k}, E)}{dE} \right] \right\} \; , \tag{2.8b}$$

and

$$T(\vec{k}, E) = [\langle \tau(E) \rangle^{-1} - B(\vec{k}, E)]^{-1} \; . \tag{2.9}$$

Here $a_0(\vec{k}, E)$ is the free-electron term, N is the number of lattice sites, and the trace operation (Tr) involves only the implicit angular-momentum indices.

Since the spectral density $a(\vec{k}, E)$ is summed over the Brillouin zone, contributions to $\langle \rho(E) \rangle$ are dominated by the singularities of the inverse matrix $T(\vec{k}, E)$ determined by the condition

$$\| \langle \tau(E) \rangle^{-1} - B(\vec{k}, E) \| = 0 \; . \tag{2.10}$$

In the case of a perfect crystal, the matrix elements $(\langle \tau_l \rangle^{-1} \delta_{LL'} - B_{LL'})$ are real and (2.10) reduces to the KKR Eq. (2.6). In the alloy, however, this matrix is complex, and for each vector $\vec{k}$ in the Brillouin zone, the secular equation (2.10) determines a sequence of complex energy levels $E_n(\vec{k}) \equiv E_n'(\vec{k}) + iE_n''(\vec{k})$. According to (2.8), these complex eigenvalues are seen to give rise to a sequence of peaks in the spectral density $a(\vec{k}, E)$; the larger the value of $E_n''(\vec{k})$, the more diffuse the corresponding structure in $a(\vec{k}, E)$. The spectrum of the alloy is thus conveniently characterized in terms of the complex energy bands defined by the alloy-KKR (AKKR) Eq. (2.10).[13] As in the perfect crystal, the size of the matrix $(\langle \tau_l \rangle^{-1} \delta_{LL'} - B_{LL'})$ is limited if the atomic phase shifts for $l \geq 3$ are neglected. Equation (2.10) then reduces to a 9×9 determinantal equation whose solution is only slightly more difficult in the alloy than in an ordered solid. A complete picture of the spectrum is, of course, given only by $a(\vec{k}, E)$ and $\langle \rho(E) \rangle$. The evaluation of these quantities, while more complicated than that of the complex energy bands, is nevertheless practical.

B. Potentials

We have used the renormalized-atom method[22] to construct l-dependent Cu and Ni potentials. The corresponding muffin-tin constants V_0^{Cu} and V_0^{Ni}, are approximately equal, and the interstitial potential in the alloy is taken as[13]

$$\bar{V}_0 = xV_0^{\mathrm{Cu}} + (1 - x)V_0^{\mathrm{Ni}} \; . \tag{2.11}$$

While this assumption fixes the muffin-tin zero of the alloy, there remains some uncertainty as to the separation of the Cu and Ni $3d$ levels. Accordingly, two different Cu potentials are employed in the present calculations. The first of these, $V_{\mathrm{I}}^{\mathrm{Cu}}$, is the same as that used in our earlier study of the CuZn system.[13] The second potential, $V_{\mathrm{II}}^{\mathrm{Cu}}$, is obtained from $V_{\mathrm{I}}^{\mathrm{Cu}}$ by empirically shifting its d muffin-tin zero. The effect of this adjustment is to raise the Cu d band by approximately 0.06 Ry. It will be seen in Sec. IV that the relative placement of the two d bands as given by V^{Ni} and $V_{\mathrm{II}}^{\mathrm{Cu}}$ is in good agreement with the results of photoemis-

TABLE I. Complex energies $(E_1, E_2) \equiv E_1 + iE_2$ in rydbergs, at symmetry points in Cu_xNi_{1-x}. The energy eigenvalues are based on the potential $V_{\mathrm{I}}^{\mathrm{Cu}}$, except when noted otherwise. The symmetry classification of energy levels is given in the first column, which also indicates whether a given alloy *d* level is derived from Cu- or Ni-like states. The energy zero is taken to be -0.8341 Ry, which is the muffin-tin zero for pure Cu. $E_d^{\mathrm{Cu(Ni)}} = \frac{1}{5}\mathrm{Re}(3E_{\Gamma_{25'}}^{\mathrm{Cu(Ni)}} + 2E_{\Gamma_{12}}^{\mathrm{Cu(Ni)}})$.

State		Cu	$Cu_{0.75}Ni_{0.25}$	$Cu_{0.75}Ni_{0.25}(V_{\mathrm{II}}^{\mathrm{Cu}})$	$Cu_{0.5}Ni_{0.5}$	$Cu_{0.25}Ni_{0.75}$	Ni
	Γ_1	0.0161	(0.0194, −0.0)	(0.0194, −0.0)	(0.0226, −0.0)	(0.0260, −0.0)	0.0295
Cu	$\Gamma_{25'}$	0.3808	(0.3822, −0.0038)	(0.4408, −0.0050)	(0.3833, −0.0077)	(0.3841, −0.0116)	
	Γ_{12}	0.4510	(0.4287, −0.0087)	(0.4844, −0.0140)	(0.4112, −0.0124)	(0.3968, −0.0144)	
Ni	$\Gamma_{25'}$		(0.5645, −0.0286)	(0.5639, −0.0286)	(0.5652, −0.0191)	(0.5661, −0.0095)	0.5672
	Γ_{12}		(0.5920, −0.0239)	(0.5950, −0.0197)	(0.6150, −0.0147)	(0.6349, −0.0070)	0.6526
Cu	X_1	0.2178	(0.2364, −0.0003)	(0.2809, −0.0002)	(0.2587, −0.0007)	(0.2884, −0.0014)	
	X_3	0.2580	(0.2765, −0.0006)	(0.3290, −0.0005)	(0.2984, −0.0016)	(0.3272, −0.0036)	
	X_2	0.4997	(0.4518, −0.0132)	(0.5003, −0.0206)	(0.4236, −0.0150)	(0.4022, −0.0155)	
	X_5	0.5165	(0.4581, −0.0148)	(0.5039, −0.0222)	(0.4270, −0.0158)	(0.4037, −0.0158)	
Ni	X_1		(0.5317, −0.0310)	(0.5389, −0.0327)	(0.4969, −0.0247)	(0.4560, −0.0188)	0.3495
	X_3		(0.5403, −0.0313)	(0.5443, −0.0327)	(0.5131, −0.0245)	(0.4793, −0.0171)	0.4172
	X_2		(0.6199, −0.0195)	(0.6303, −0.0133)	(0.6560, −0.0123)	(0.6853, −0.0060)	0.7108
	X_5		(0.6312, −0.0181)	(0.6444, −0.0117)	(0.6710, −0.0116)	(0.7029, −0.0058)	0.7308
	$X_{4'}$	0.8372	(0.8369, −0.0)	(0.8369, −0.0)	(0.8366, −0.0)	(0.8363, −0.0)	0.8361
Cu	L_1^l	0.2347	(0.2516, −0.0003)	(0.2926, −0.0002)	(0.2721, −0.0009)	(0.2993, −0.0017)	
	L_3^l	0.3739	(0.3780, −0.0035)	(0.4361, −0.0044)	(0.3805, −0.0073)	(0.3827, −0.0113)	
	L_3^u	0.5028	(0.4531, −0.0135)	(0.5010, −0.0209)	(0.4243, −0.0152)	(0.4025, −0.0156)	
Ni	L_1^l		(0.5293, −0.0304)	(0.5374, −0.0324)	(0.4939, −0.0240)	(0.4538, −0.0183)	0.3572
	L_3^l		(0.5626, −0.0288)	(0.5621, −0.0291)	(0.5612, −0.0194)	(0.5600, −0.0098)	0.5591
	L_3^u		(0.6218, −0.0192)	(0.6327, −0.0130)	(0.6586, −0.0121)	(0.6883, −0.0060)	0.7143
	$L_{2'}$	0.6193	(0.6187, −0.0)	(0.6187, −0.0)	(0.6181, −0.0)	(0.6174, −0.0)	0.6168
	L_1^u	1.0018	(1.0381, −0.0025)	(1.0554, −0.0016)	(1.0722, −0.0031)	(1.1045, −0.0021)	1.1354
	E_d^{Cu}	0.4088	0.4008	0.4582	0.3945	0.3892	
	E_d^{Ni}		0.5755	0.5763	0.5851	0.5936	0.6014

sion measurements. It should be emphasized that discrepancies on the order of 1 eV in the positioning of the *d* bands are quite common in first-principles calculations of transition and noble-metal band structures. For this reason, previous authors[36,37] have often employed empirical adjustments of the kind we have described.

The fact that neutral-atom potentials for both Cu and Ni are being used in the present calculations is consistent with the familiar minimum-polarity model for CuNi alloys.[38] In CuNi the variation of the lattice constant with alloy composition is small.[39] In the present calculations, as in those of Refs. 8 and 9, the lattice constant of the alloy Cu_xNi_{1-x} was taken equal to that of pure Cu (i.e., $a = 6.8309$ a.u.).

III. ELECTRONIC ENERGY SPECTRUM

A. Complex energy bands

The results of our calculations are summarized in Table I and Fig. 1. Table I gives the low-lying complex energy eigenvalues at the symmetry points Γ, *X* and *L*, in paramagnetic Cu_xNi_{1-x} over the entire composition range. A typical plot of the complex energy bands along the principal symmetry directions is shown in Fig. 1. Here the imaginary part of the eigenvalues is represented by shading of vertical length $2\,\mathrm{Im}\,|E_n(\vec{k})|$ around each band.

Most of the results presented in this paper employ the potential $V_{\mathrm{I}}^{\mathrm{Cu}}$. In understanding the qualitative features of the CuNi spectrum, the differences between $V_{\mathrm{I}}^{\mathrm{Cu}}$ and $V_{\mathrm{II}}^{\mathrm{Cu}}$ are relatively unimportant. For completeness, however, some representative results for the complex energy levels obtained using $V_{\mathrm{II}}^{\mathrm{Cu}}$ are shown in Table I. As noted earlier, the most important effect of this adjustment is to raise the Cu *d* band by roughly 0.06 Ry. Reference to columns 3 and 4 of Table I shows further that this shift of the Cu *d* band is approximately rigid, i.e., the widths of the constituent *d* bands [as monitored, for example, by $(E_{X_5} - E_{X_3})$] are unaffected to within 10%. The imaginary parts, however, are somewhat more sensitive.

Figure 1 shows that two sets of *d* bands are present in the CuNi spectrum. The upper and the lower sets arise, respectively, from the Ni and Cu *d* states. Within the framework of a single-

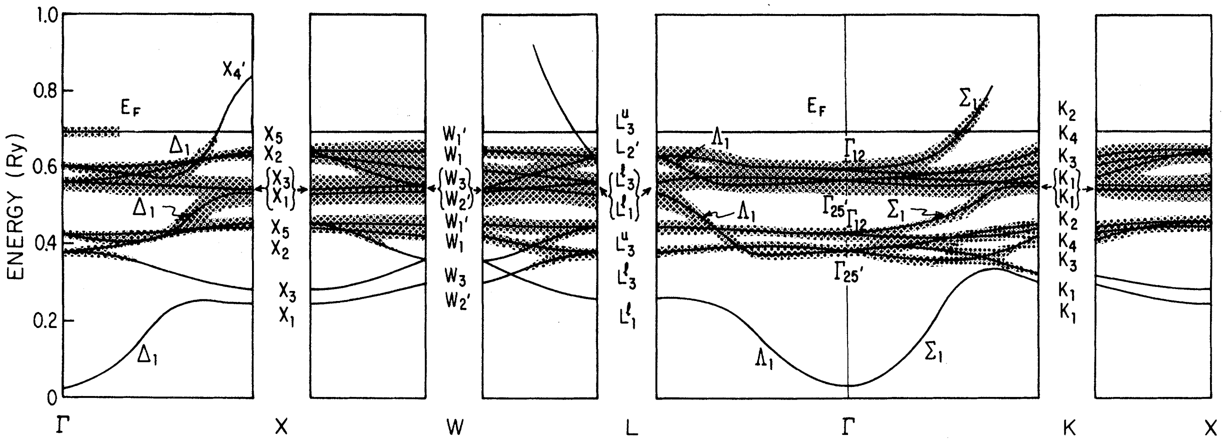

FIG. 1. Complex energy bands for $Cu_{0.7}Ni_{0.3}$ (Ref. 40). The shading of the bands corresponds to twice the imaginary part of the complex energies. (The shading around the Fermi energy represents the average damping on the Fermi surface.) The energy zero is taken to be -0.8341 Ry, which is the muffin-tin zero for pure Cu.

site approximation, we recall that the disordered alloy is replaced by a periodic crystal of effective complex potentials. The labeling of energy levels in the alloy is thus identical to that in an ordered fcc transition metal. In particular, in the alloy, just as in the perfect crystal, the size of the secular determinant [Eq. (2.10)] at symmetry points in the Brillouin zone can be reduced. As discussed in the Appendix, this fact is useful in separating and identifying closely placed levels in the alloy.

The general behavior of the bands can be understood on the basis of symmetry considerations. We focus on the $\Gamma\rightarrow X$ panel in Fig. 1. Note, first, that there are two sets of d bands (terminating at X_3, X_2, and X_5) which do not hybridize with the conduction band. This behavior is characteristic of fcc transition metals where only the single d band of symmetry Δ_1 is allowed to interact with the conduction band. In the present case we have a two-d-band system and, therefore, two sets of unhybridized d levels. Turning next to the hybridizing bands in Fig. 1, we note that the upper and lower Δ_1 bands are similar in structure to those appearing in ordered transition metals. In addition, the alloy contains a *third* Δ_1 band, which begins as a Cu level (Γ_{12}) and ends as a Ni level (X_1). In Cu this band would have terminated at $X_{4'}$, but here it undergoes a hybridization with the Ni d bands. A similar pattern of hybridized and unhybridized levels is repeated in the other panels of Fig. 1. Thus even in the present case where ten d bands intersect a common conduction band, the classification of the quasiparticle states is surprisingly simple.

Consider next, the imaginary parts of the complex bands. Figure 1 shows that the conduction states are essentially undamped. This is to be expected since the s-p potentials of Cu and Ni used in the present calculations are similar. For example, the levels Γ_1 and $X_{4'}$ in Cu and Ni differ by less than 0.02 Ry. By contrast, the damping of the d states is strongly energy dependent. The d states at the lowest energies (e.g., X_1, X_3, L_1^{ℓ}) are essentially undamped, while those at higher energies show substantial broadening.

While the complex bands are of interest, a complete description of the alloy spectrum requires the evaluation of the spectral density $a(\vec{k},E)$ and the density of states $\langle\rho(E)\rangle$. The behavior of the spectral density at Γ and X is illustrated in Fig. 2 for $Cu_{0.7}Ni_{0.3}$. The real and imaginary parts of the corresponding energy levels are also shown along the energy axis. Consider, first, Fig. 2(a). The state Γ_1 is essentially undamped, and as expected, this level leads to a very sharp peak in the spectral density. The half-widths of the Cu d states (the lower pair Γ_{12}, $\Gamma_{25'}$) are small compared to their damping, and these states are seen to give a distinct doublet. By contrast, the damping of the Ni d levels (the upper pair Γ_{12}, $\Gamma_{25'}$) is of the same order as their separation, and the resulting peaks are barely resolved. The details of the structure in Fig. 2(b), which refers to the symmetry point X, can be understood similarly. These results show that the real and imaginary parts of the complex bands correspond quantitatively to the detailed structure of $a(\vec{k},E)$. Calculations at additional points in the Brillouin zone bear this out and provide further justification for describing the alloy quasiparticle spectrum in terms of the complex band structure.[14] Finally, we note that the spectral density function $a(\vec{k},E)$ given by Eq. (2.8) is always found to be positive definite.[41] By contrast, the density-of-states

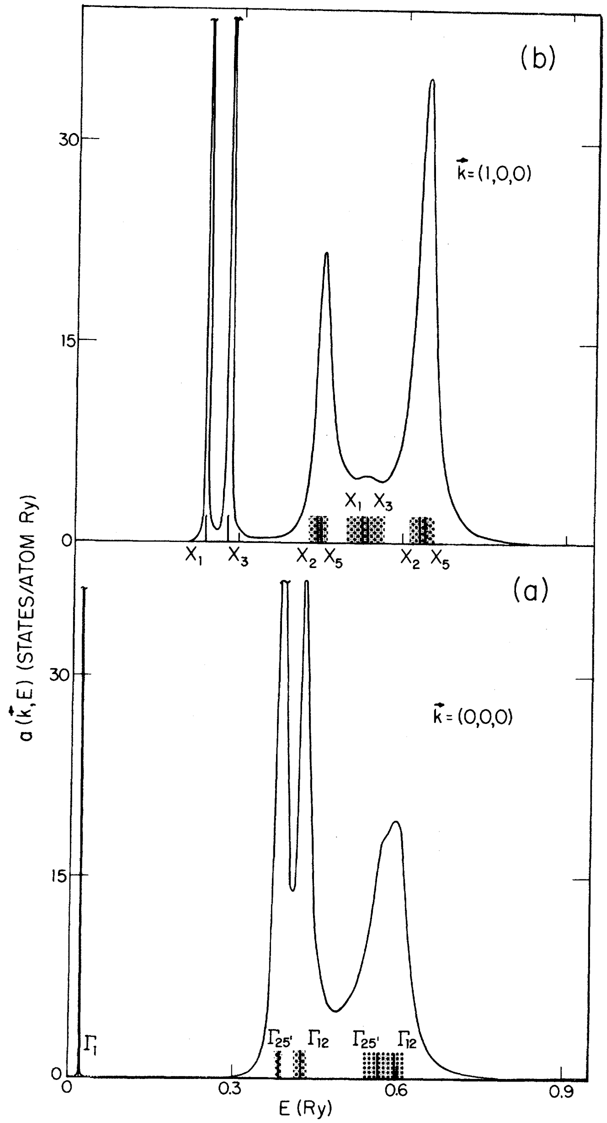

FIG. 2. Spectral density of states $a(\vec{k},E)$ for $Cu_{0.7}Ni_{0.3}$ at two symmetry points: (a) $\vec{k}=(0,0,0)$, and (b) $\vec{k}=(1,0,0)$. The shading of the complex levels, shown on the horizontal axis, corresponds to $2\,|\,\mathrm{Im}E_n(\vec{k})\,|$.

formalism of Ref. 16 does not satisfy this requirement.

A peak in the spectral density function can be described in terms of three parameters: its location, width, and weight. The preceding discussion shows that in the alloy, the complex eigenvalues represent accurately two of these, i.e., the position and width. The assignment of a unit weight to *each* $\vec{k}$ state, as in a perfect crystal, is obviously incorrect in the alloy.

B. Density of states

Using Eq. (2.8), we have evaluated the electronic density of states in paramagnetic Cu_xNi_{1-x} for several concentrations x. The *special directions* method was employed to carry out the $\vec{k}$-space integrations in (2.8a). (A brief summary of the numerical techniques is given in the Appendix.) A set of 13 special directions was used in the present calculations and the results were smoothed over an energy interval of approximately 0.005 Ry.[20]

The computed densities of states for three alloy compositions and both the pure constituents are shown in Fig. 3. To begin, let us compare the pure Cu spectrum with that of the Cu-rich alloy

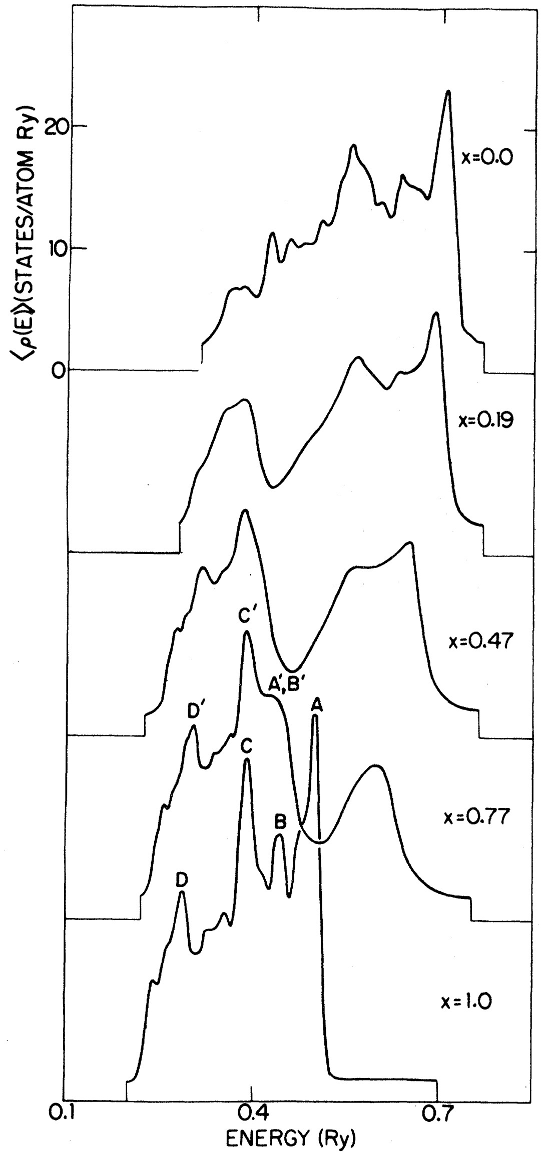

FIG. 3. Densities of states $\langle\rho(E)\rangle$ in the alloy Cu_xNi_{1-x} (Ref. 40). The successive curves are shifted with respect to each other by a constant amount on the vertical scale. The energy zero is given as in Fig. 1.

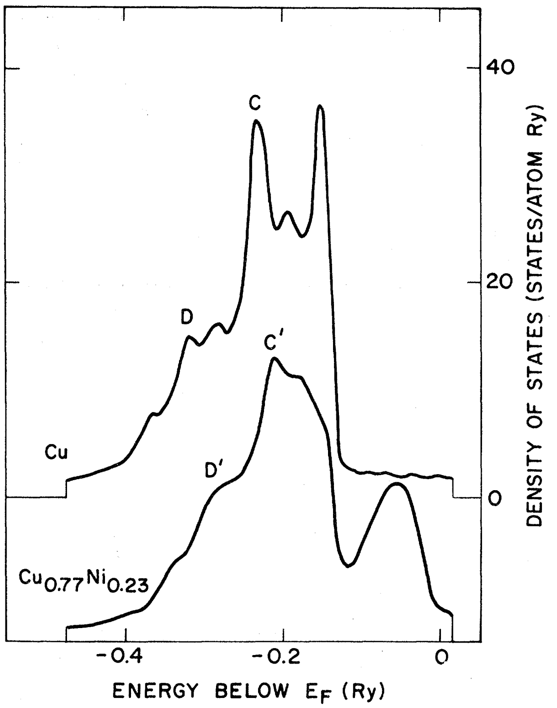

FIG. 4. Densities of states in Cu and $Cu_{0.77}Ni_{0.23}$, reproduced from Ref. 9. For this comparison, the energy zero of the alloy density of states given in Ref. 9 has been shifted such that the sharp edges in the two curves at ≈ -0.14 Ry coincide.

$Cu_{0.77}Ni_{0.23}$. The most pronounced effect of alloying is the appearance of a relatively structureless subband associated with the Ni d states.[8,9,23] The variation of this subband with Ni concentration will be discussed in Sec. IV B. We focus here on the Cu subband and compare its structure (in particular, the peaks labeled A', B', C', D') with the associated structure in pure Cu (i.e., the peaks A, B, C, D). The peaks A, B, and C are most affected by the alloying process. Indeed, A and B are reduced to an edge (A', B'). This is due to the heavy damping of the corresponding states as monitored, for example, by states in the vicinity of the lower X_5, X_2, and Γ_{12} levels in Fig. 1. While the peak C persists in the alloy, it is broader than its counterpart in pure Cu. By contrast, because the low-energy part of the alloy Cu d band is essentially undamped (cf. Fig. 1), the structure at D is relatively unaffected. This behavior is absent in the model Hamiltonian calculations of Ref. 9 where the electron self-energies are assumed to be $\vec{k}$ independent. As shown in Fig. 4, the Cu peaks C and D smooth rapidly with increasing Ni concentration.[42] The photoemission experiments to be discussed in Sec. IV appear to favor the present calculations in this respect.

Consider next the results for $Cu_{0.47}Ni_{0.53}$ and $Cu_{0.19}Ni_{0.81}$. In going from the Cu to the Ni-rich regime, the Ni subband is seen to increase in weight and to develop structure at the expense of its Cu counterpart. Furthermore, in accord with the predictions of the model Hamiltonian calculations, the Cu d states are seen to have a less pronounced effect on the alloy spectrum in the Ni-rich regime than the Ni d states have in the Cu-rich case. This behavior is seen more clearly by comparing the corresponding results based on the potential V_{II}^{Cu} (cf. Figs. 10 and 11) and is primarily due to the asymmetry of the d-band density of states in an fcc transition metal. The differences between the Cu-rich and Ni-rich regimes are also apparent in the complex energy bands. Thus the outside panels of Fig. 5 show that the center of the Ni d resonance lies well *above* the top of the Cu d bands, while the Cu resonance lies *within* the lower part of the Ni d bands. It is then clear that the impurity structure will be more pronounced in the Cu-rich limit.

IV. COMPARISON WITH EXPERIMENT

A. Alloy density of states

Our calculated densities of states are compared in Figs. 6–10 with the corresponding photoemission and XPS measurements of Krolikowski and Spicer (Cu),[27] Eastman and Krolikowski[26] and Seib and Spicer (Ni),[24] Seib and Spicer[24] ($Cu_{0.77}Ni_{0.23}$ and $Cu_{0.19}Ni_{0.81}$), and Hüfner *et al.*[25] ($Cu_{0.47}Ni_{0.53}$).

The measurements in Refs. 24, 26, and 27 were made with incident photon energies on the order of 10 eV. At these low energies the electrons penetrate only a few atomic layers, and the extent to which they sample the bulk properties of the materials is not clear.[43] An additional complication arises from the fact that the photoemission process involves interband electronic transitions and therefore the joint density of states $N(E, h\nu)$. The valence-band-state density $\rho_v(E)$ can be separated from that for the conduction band $\rho_c(E)$ simply only if it is assumed[44-48] that $N(E, h\nu) \sim \rho_c(E)\rho_v(E$

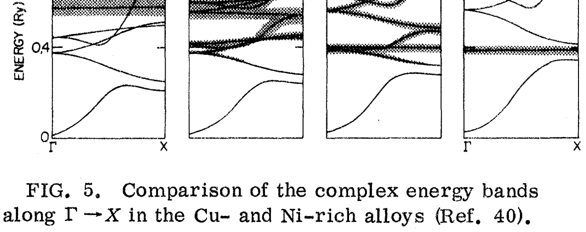

FIG. 5. Comparison of the complex energy bands along $\Gamma \to X$ in the Cu- and Ni-rich alloys (Ref. 40). Shading conventions are as in Fig. 1.

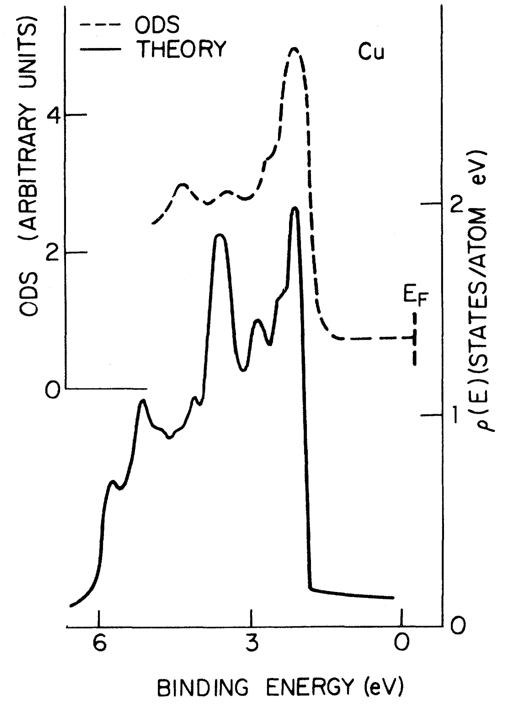

FIG. 6. Comparison of the computed density of states in Cu (employing $V_{\rm II}^{(\rm Cu)}$) with the photoemission optical density of states (ODS) obtained by Krolikowski and Spicer (Ref. 27). The energy zero for the experimental curve has been shifted so that the high-energy peaks in the two curves coincide. The binding energy for the theoretical curve is measured with respect to the Fermi energy.

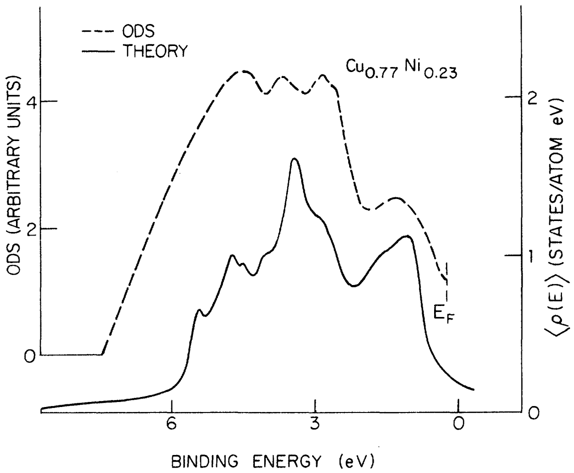

FIG. 7. Comparison of the computed density of states in the Cu-rich alloy $Cu_{0.77}Ni_{0.23}$ (employing $V_{\rm II}^{(\rm Cu)}$) with the optical density of states (ODS) obtained by Seib and Spicer (Ref. 24). The energy zero of the experimental curve has been shifted so that the edges of the two Cu subbands, which occur at a binding energy of ≈2.5 eV, coincide.

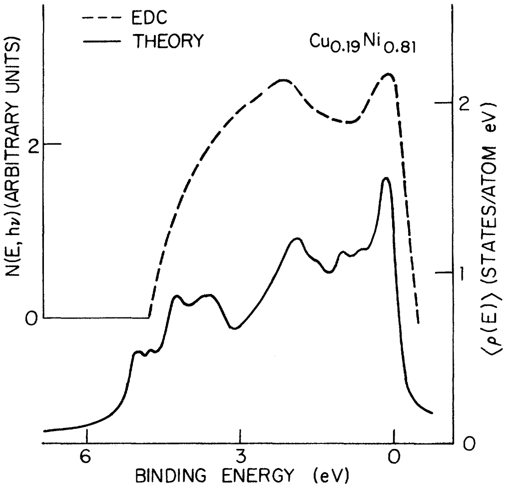

FIG. 8. Comparison of the computed density of states in the Ni-rich alloy $Cu_{0.19}Ni_{0.81}$ (employing $V_{\rm II}^{(\rm Cu)}$) with the photoemission-energy-distribution curve (EDC) of Seib and Spicer (Ref. 24) (taken at photon energy, $h\nu = 10$ eV). The energy zero of the experimental curve has been shifted so that the high-energy peaks in the two curves coincide.

$-h\nu$) and that ρ_c is relatively structureless compared to ρ_v. The comparison of experimental energy distribution curves (EDC's) for small $h\nu$ with theory is therefore not entirely satisfactory. This difficulty does not appear to occur for $h\nu \gtrsim 50$ eV

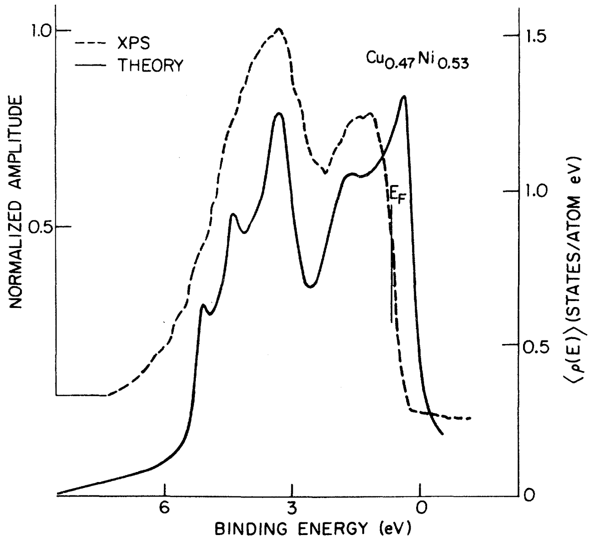

FIG. 9. Comparison of the computed density of states in $Cu_{0.47}Ni_{0.53}$ (employing $V_{\rm II}^{(\rm Cu)}$) with the x-ray-photoemission measurements of Hüfner *et al.* (Ref. 25). The energy zero of the experimental curve has been shifted so that the edges of the two Cu subbands which occur at a binding energy of ≈3 eV coincide.

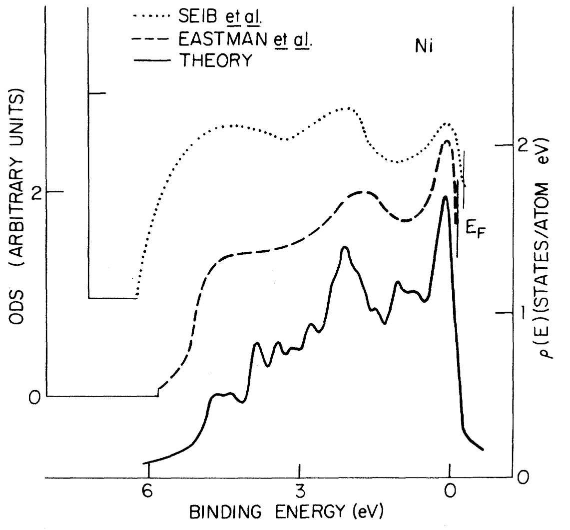

FIG. 10. Comparison of the computed density of states in Ni with the photoemission optical density of states obtained by Seib and Spicer (Ref. 24) (dotted), and Eastman and Krolikowski (Ref. 26) (dashed). The energy zeros of the experimental curves have been shifted so that the high-energy peaks in the theoretical and experimental curves coincide.

where experimental observations[43] indicate that the structure of the EDC's becomes independent of $h\nu$, presumably because it reflects only $\rho_v(E)$.

Both curves in Fig. 7 for the Cu-rich alloy $Cu_{0.77}Ni_{0.23}$ show a pronounced subband due to the Ni d states. We focus here on the structure of the Cu subband. A comparison of Figs. 6 and 7 shows two changes in the experimental optical density of states (ODS) of Cu resulting from the addition of 23-at.% Ni. (i) The sharp peak at approximately 2 eV in the pure Cu ODS is substantially smoothed in the alloy. (ii) By contrast, the structure at lower energies (i.e., from roughly 3 to 6 eV) remains relatively unchanged. These features are reproduced in the theoretical curves of Figs. 6 and 7.

In the Ni-rich alloy $Cu_{0.19}Ni_{0.81}$ (Refs. 49–51) (Fig. 8), the Cu impurities have a much less pronounced effect on the density of states than do the Ni impurities in the Cu-rich alloy, as expected. Indeed, the structure due to the Cu d states in the theoretical curve of Fig. 8 is not resolved in the experimental data.

The density of states in the nearly equiatomic alloy $Cu_{0.47}Ni_{0.53}$ is compared with XPS measurements in Fig. 9. [The data reproduced from Ref. 25 have been corrected for inelastic components but not for instrumental resolution (roughly 0.55 eV—full width at half-maximum).] The qualitative features of the two curves are in substantial agreement. Both exhibit well-defined Cu and Ni subbands, and the structure within the individual subbands, although smoothed, is quite noticeable in the experimental curves. The observed width of the Ni subband, however, is less than the theoretical prediction by roughly 0.5 eV. This is not surprising since the XPS results for pure Ni are known to give a d bandwidth which is too narrow by approximately 1 eV.[25] While this discrepancy has been ascribed to many electron and surface effects, its explanation remains a matter of controversy.[52]

B. Ni virtual bound state (VBS)

The theoretical definition of the half-width of the Ni VBS is complicated by the fact that the d-band density of states in an fcc crystal peaks at high energies (cf. Fig. 3). We have already discussed the effects of this asymmetry on the influence of the minority component on the density of states in the Cu- and Ni-rich limits. As a further consequence, Fig. 7 shows that the shape of the Ni VBS is not symmetric, i.e., that its left-hand-side and right-hand-side half-widths are unequal. In addition, we note that the left part of the VBS overlaps with the Cu d band and is less well resolved in the photoemission experiments. For these reasons, we will be concerned with the *right-hand-side half-width at half-maximum* in the following comparison of theory and experiment.

There are two important contributions to the half-width of the Ni VBS. The first of these, $\Delta_d^{(r)}$, is associated with the spread in energy of the *real* parts of the Ni d bands. Physically, this spread is due to the hopping of the d electrons between neighboring Ni atoms and also to the coupling of the Ni d states with the conduction band. In the present context we are interested not in the total width of the fcc d band, but rather in the part of the bandwidth due to the high density-of-states region enclosed by the t_{2g} peaks A and C in Fig. 3. The positions of these peaks are monitored, respectively, by the levels X_5 and $\Gamma_{25'}$ (cf. the results for pure Cu in Table I and Fig. 3). $\Delta_d^{(r)}$ can then be estimated as

$$\Delta_d^{(r)} \approx \tfrac{1}{2}\mathrm{Re}(E_{X_5} - E_{\Gamma_{25'}}) . \tag{4.1}$$

The second contribution to the half-width, $\Delta_d^{(i)}$, is due to the *imaginary parts* (i.e., to broadening) of the individual Ni d levels. Since we are again primarily concerned with the right-hand-side half-width, $\Delta_d^{(i)}$ will be estimated as[53]

$$\Delta_d^{(i)} \approx \mathrm{Im}(E_{X_5}) . \tag{4.2}$$

In Fig. 11, the complex energy bands along the [100] direction are shown for several Cu-rich alloys. The limiting nature of the Ni d resonance is presented in Fig. 12. Figures 11 and 12 show that as the Ni concentration is decreased, the con-

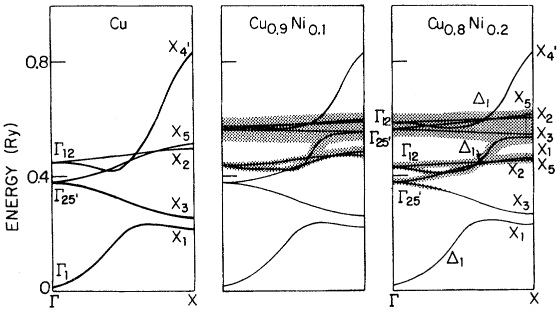

FIG. 11. Concentration dependence of the complex energy bands along $\Gamma \rightarrow X$ in Cu-rich alloys (Ref. 40). Shading conventions are as in Fig. 1.

tribution due to the splitting of the real parts approaches zero, and the half-width of the VBS is dominated by the broadening of the Ni d levels.

In Fig. 13 we consider the concentration dependence of $\Delta_d^{(r)}$, $\Delta_d^{(i)}$, and $\Delta_d \equiv \Delta_d^{(r)} + \Delta_d^{(i)}$. The values of Δ_d are in good agreement with the right-hand-side half-widths of the Ni d peaks in the corresponding density-of-states curves, some of which are shown in Fig. 14.[54] Shown also in Fig. 13 are other available estimates for the Ni VBS half-width. Between 10- and 30-at.% Ni, our results are in substantial agreement with the experimental measurements of Seib and Spicer[24] and Hüfner *et al.*[25] As already noted, the model Hamiltonian calculations of Ref. 9 will lead to a vanishing VBS half-width in the limit of zero-Ni concentration. Below 10-at.% Ni, no photoemission data is currently available. There are, however, other far more indirect experimental estimates of Δ_d in this concentration range which are also shown in Fig. 13. In the limit of zero-Ni concentration, our calculations predict a VBS half-width of 0.04 Ry, with an uncertainty on the order of 0.01 Ry. The values obtained by Foiles[55] were derived by comparing the theory with experimental thermoelectric power (TEP) data on CuNi alloys. This procedure, however, is sensitive to the choice of the VBS peak shape. The same is true for the estimate of Klein and Heeger,[56] based on specific-heat and residual-resistivity measurements. The point at 4% corresponds to a width deduced from optical-absorption measurements.[28] The implied value of Δ_d turns out to be smaller than that given by the present calculations by approximately a factor of 2. We emphasize, however, that the relation between optical-absorption measurements and the average single-particle density of states in the alloy is somewhat ambiguous. Detailed photoemission measurements for Ni concentrations below 5 at.% would be helpful in clarifying the behavior of the Ni VBS half-width.

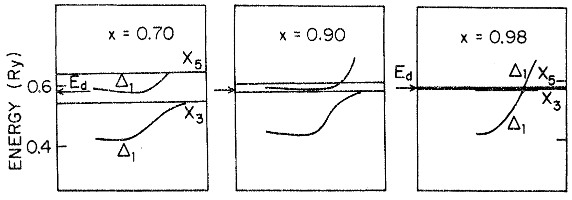

FIG. 12. Concentration dependence of the splitting of the Ni d levels in Cu-rich Cu_xNi_{1-x}. The damping of the energy levels is not shown. The arrow at the left-hand side of each panel marks the position of the center of gravity of the Ni subband defined by $E_d = \frac{1}{5}\mathrm{Re}(3E^{\mathrm{Ni}}_{\Gamma_{25'}} + 2E^{\mathrm{Ni}}_{\Gamma_{12}})$. In the limiting case ($x = 0.98$), both the separation between X_5 and X_3 and the hybridization splitting between the two Δ_1 bands approach zero.

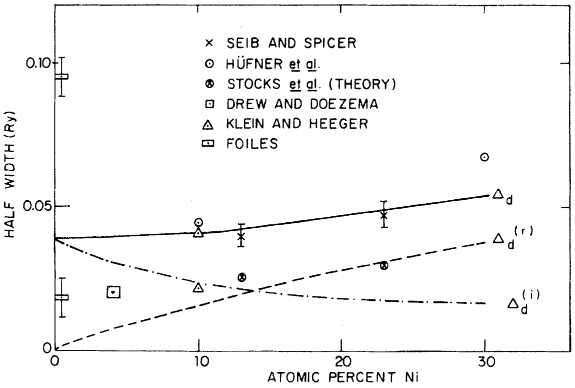

FIG. 13. Comparison of the calculated half-width Δ_d of the Ni virtual bound state with available estimates. (See text for details of data points.) The two components $\Delta_d^{(r)}$ and $\Delta_d^{(i)}$ of the half-width are also plotted.

C. Fermi-surface properties

In this subsection we compare our calculations with the available experimental data on the Fermi-surface properties of Cu-rich CuNi alloys. As seen from Figs. 1 and 11, the Ni d bands in the Cu-rich alloy do not intersect the Fermi level. The alloy Fermi surface is, therefore, comprised of a single sheet as in pure Cu. By contrast, in the Ni-rich regime, the Ni d levels intersect E_F, and the resulting Fermi surface consists of several sheets. This more complicated case will not be discussed here.

We consider first the Fermi-surface radii k_{100}, k_{110}, and k_N (cf. Table II). For low Ni concentrations, the present results deviate substantially from the predictions of the rigid-band model,[32] where the Cu_xNi_{1-x} Fermi surface is obtained by filling the pure-Cu band structure with $11x + 10(1-x) = 10 + x$ electrons per atom. The rigid-band model predicts a *decrease* in k_N of 3.0%/at.% Ni,

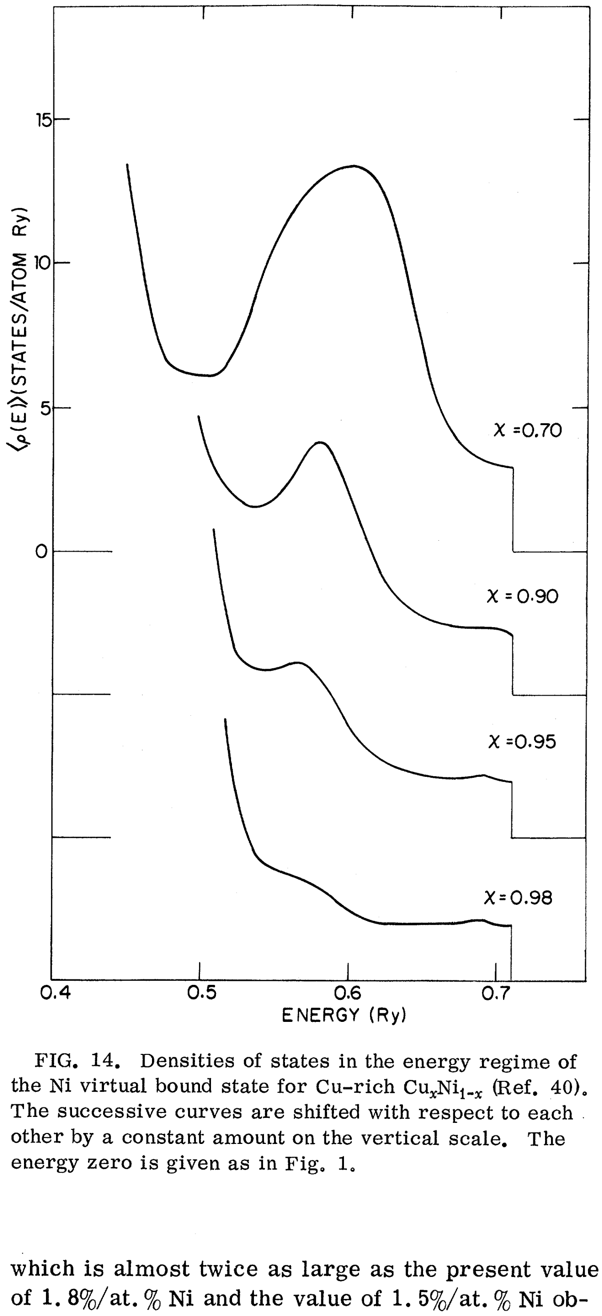

FIG. 14. Densities of states in the energy regime of the Ni virtual bound state for Cu-rich Cu_xNi_{1-x} (Ref. 40). The successive curves are shifted with respect to each other by a constant amount on the vertical scale. The energy zero is given as in Fig. 1.

which is almost twice as large as the present value of 1.8%/at.% Ni and the value of 1.5%/at.% Ni obtained from the de Haas-van Alphen measurements of Coleridge and Templeton.[29] We note further that the deviations from the rigid-band model increase for larger Ni concentrations. In fact, the rigid-band model predicts $k_N \to 0$ at 30%-Ni concentration, while our calculations imply a decrease in k_N of only 23%. The present results are in general agreement with the positron-annihilation measurements of Rouse and Varlashkin[31] in which no substantial change in k_N as a function of Ni concentration was observed.

The conduction bands (i.e., the upper Δ_1 bands in Fig. 11) in $Cu_{0.9}Ni_{0.1}$ and $Cu_{0.7}Ni_{0.3}$ enclose volumes in the Brillouin zone corresponding, respectively, to 0.93 and 0.79 electrons per atom. These numbers are reasonably close to the rigid-band values of 0.9 and 0.7 electrons per atom. Nevertheless, this fact should not be taken to imply the validity of the rigid-band model. Unlike the situation in a perfect crystal, the complex eigenvalues $E_n(\vec{k})$ in the alloy do not contribute to the spectrum with unit weight. In general, one cannot deduce the number of conduction electrons per atom from just the Fermi-surface dimensions of transition and noble-metal alloys.

In the dilute limit (i.e., impurity concentrations on the order of a few tenths of an atomic percent), the average damping of electronic states on specific orbits of alloy Fermi surface is given by de Haas-van Alphen Dingle-temperature experiments.[29] [In alloys with higher concentrations, the broadening of Fermi-surface states can, in principle, be obtained by positron annihilation or Compton scattering techniques. Unfortunately, the resolution presently available in these experiments does not permit such measurements.[57]] The most recent values for the Dingle temperatures[30] x_N and x_B of the neck and ⟨111⟩ belly orbits in CuNi are $x_N = 14.9$ and $x_B = 30.9$ °K/at.% Ni. These are in excellent agreement with the corresponding calculated values $x_N = 15.5$ and $x_B = 30.6$ °K/at.% Ni. The calculations show that the Fermi-surface damping anisotropy is dominated by the difference between the Cu and Ni d potentials.[58]

The preceding results are based on the potential $V_{\rm I}^{\rm Cu}$. The Fermi-surface radii k_{100}, k_{110}, and k_N are insensitive to the use of $V_{\rm II}^{\rm Cu}$, especially insofar as the changes in the various radii as a function of Ni concentration are concerned. By contrast, the damping at the Fermi surface decreases by 30 to 40% if $V_{\rm II}^{\rm Cu}$ is employed. This would imply a similar reduction in the Dingle tem-

TABLE II. Fermi-surface properties of Cu-rich CuNi alloys (Ref. 40). The belly radii k_{100} and k_{110} and the neck radii k_N are given in units of $(2\pi/a)$, where a is the cube edge of the fcc Cu lattice. The values of the average dampings are given in rydbergs.

	Cu	$Cu_{0.9}Ni_{0.1}$	$Cu_{0.7}Ni_{0.3}$
Fermi-surface radii			
k_{100}	0.815	0.808	0.796
k_{110}	0.744	0.718	0.657
k_N	0.155	0.135	0.119
Average dampings			
Fermi surface	0.0	−0.0047	−0.0090
⟨111⟩ Belly	0.0	−0.0050	−0.0095
⟨111⟩ Neck	0.0	−0.0029	−0.0065

peratures. A general decrease in the damping is expected when the Cu d band is moved closer to the Ni d band, because the resulting Cu and Ni potentials become more similar.

ACKNOWLEDGMENTS

We acknowledge useful communications from H. D. Drew, W. E. Spicer, and G. K. Wertheim. We have also benefitted from conversations with S. Berko, J. S. Faulkner, C. D. Gelatt, Jr., and R. J. Higgins.

APPENDIX: NUMERICAL TECHNIQUES

The numerical techniques pertaining to the computation of the complex roots of the AKKR Eq. (2.10) and the density of states in the alloy are presented in this appendix.

In Ref. 13, the complex roots were obtained by fitting the AKKR determinant to an appropriate monomial in the vicinity of the solution. This procedure is not suited to calculating closely placed energy levels (as in the case of the Ni d levels in Cu-rich CuNi alloys), and furthermore, it does not allow a direct identification of the symmetry label of a given root. To illustrate how these difficulties can be overcome at $\vec{k}$ points of high symmetry, consider the levels Γ_1, $\Gamma_{25'}$, and Γ_{12}. In the case of pure Cu, each of these energy levels can be obtained by solving a (1×1) subdeterminant (if phase shifts for only $l \leq 2$ are used). In the CuNi alloy, it follows that the *same* subdeterminants of the AKKR matrix will yield two sets of levels Γ_{12} and $\Gamma_{25'}$, and a single unsplit level Γ_1. The calculation of the complex bands at other points of high symmetry can be simplified in a similar manner.

In contrast with the case of complex energy bands, the computation of the spectral density $a(\vec{k}, E)$ (cf. Eq. (2.8) and Fig. 2) requires the structure functions $B_{LL'}(\vec{k}, E)$ and the atomic scattering matrices $\tau^{A(B)}$ only at real energies. Once $a(\vec{k}, E)$ is known, the calculation of $\langle\rho(E)\rangle$ is quite straightforward. The necessary $\vec{k}$-space integration can be carried out efficiently by using the *special directions* technique.[20] In practice, it is better to compute the integrated density of states $N(E)$ first and then to calculate $\langle\rho(E)\rangle$ by differentiation. To this end we cast Eq. (2.8) into the form

$$\langle\rho(E)\rangle = \rho_0(E) - (\pi N)^{-1}\,\mathrm{Im}\sum_{\vec{k}} \frac{d}{dE}\ln\|A(\vec{k}, E) + \kappa C(E)\| - (\pi N)^{-1}\,\mathrm{Im}\,\mathrm{Tr}\Big[\sum_{\vec{k}} \kappa[A(\vec{k}, E) + \kappa C(E)]^{-1}(i - C)\Big(x\frac{d}{dE}\ln(C^B - C) + y\frac{d}{dE}\ln(C^A - C) - \frac{d}{dE}\ln(C^A - C^B)\Big)\Big] \; . \tag{A1}$$

Here we have used the real structure functions $A_{LL'}(\vec{k}, E)$ and the cotangents of the phase shifts $C_l^{A(B)}$, defined by the equations

$$B_{LL'} = A_{LL'} + i\kappa\delta_{LL'} \tag{A2a}$$

and

$$(\tau_l^{A(B)})^{-1} = i\kappa - \kappa C_l^{A(B)} \; . \tag{A2b}$$

Similarly,

$$\langle\tau_l\rangle^{-1} = i\kappa - \kappa C_l \; . \tag{A2c}$$

Equation (A1) immediately yields

$$N(E) = N_0(E) - (\pi N)^{-1}\,\mathrm{Im}\sum_{\vec{k}} \ln\|A(\vec{k}, E) + \kappa C(E)\| - (\pi N)^{-1}\,\mathrm{Im}\,\mathrm{Tr}\int_0^E dE\,\Big[\sum_{\vec{k}} \kappa[A(\vec{k}, E) + \kappa C(E)]^{-1}(i - C) \times\Big(x\frac{d}{dE}\ln(C^B - C) + y\frac{d}{dE}\ln(C^A - C) - \frac{d}{dE}\ln(C^A - C^B)\Big)\Big] \tag{A3}$$

$$= \sum_{\vec{k}} N(\vec{k}, E) \tag{A4a}$$

$$\equiv \sum_{\vec{k}} [N_0(\vec{k}, E) + N_1(\vec{k}, E) + N_2(\vec{k}, E)] \; . \tag{A4b}$$

Here $N(\vec{k}, E)$ represents the spectral decomposition of $N(E)$. The N_0 term gives the free-electron contribution, and N_1 and N_2, respectively, denote the second and third terms on the right-hand side of Eq. (A3).

The evaluation of the phase of the logarithm in

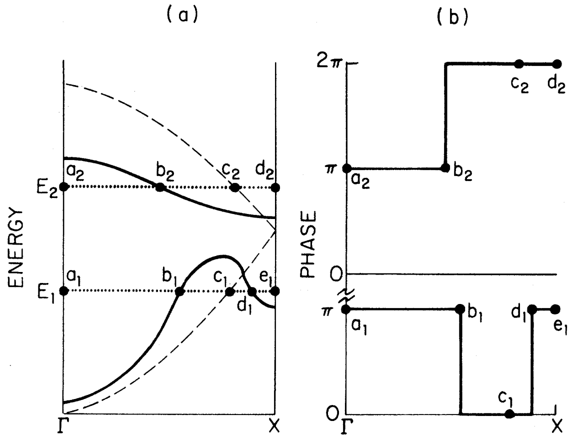

FIG. 15. Energy bands for a *hypothetical* perfect crystal (solid) and free electrons (dashed) are shown along $\Gamma \rightarrow X$ in Fig. 15(a). The variation of the phase $N_1(\vec{k}, E)$ (Ref. 59) [cf. Eq. (A4b)], at two energies E_1 and E_2 as one proceeds from $\Gamma \rightarrow X$ [i.e., along horizontal dotted lines in Fig. 15(a)], is shown in Fig. 15(b).

$N_1(\vec{k}, E)$ in Eq. (A4) requires care and may be illustrated by specializing to the case of a pure crystal. Note that in this limit $N_2(\vec{k}, E)$ vanishes identically, and that the quantity $\| A(\vec{k}, E) + \kappa C(E) \|$ is real except in the vicinity of the eigenvalues. The phase of the logarithm in $N_1(\vec{k}, E)$ must therefore be incremented by $n\pi$ when an n fold root is crossed. Consequently, n sign changes must be associated with an n-fold eigenvalue. It is clear that the phase in question cannot be computed by simply taking the logarithm of $\| A + \kappa C \|$ because this quantity, being a scalar number, will show only one sign change at an odd root and no sign change at a root of even degeneracy. The simplest way out of this problem is to diagonalize the KKR matrix and compute the overall phase as the *sum of the phases* of the diagonal elements.

So far we have not dealt with the question of free-electron singularities. These are present in both the N_0 and N_1 terms in Eq. (A3) and can be shown to cancel each other.[15] Consequently, these singularities should be omitted in computing the phase $N_1(\vec{k}, E)$. This can be achieved by subtracting π times the number of free-electron roots below E (for a given $\vec{k}$) from the overall phase of $N_1(\vec{k}, E)$.

The preceding discussion can be clarified by considering as an illustrative example the *hypothetical* solid whose energy bands are shown in Fig. 15(a) (shown also are the free-electron roots). The variation of the phase $N_1(\vec{k}, E)$ (Ref. 59) in going from Γ to X is shown in Fig. 15(b) at two typical energies (labeled E_1 and E_2). Figure 15(b) shows that at the point Γ, the phase is taken to be π (and not 2π), because the free-electron roots must not be counted. Accordingly, the phases are continuous through the cross-over points with free-electron bands (such as c_1 and c_2). Note also that the lower full band contributes a uniform phase of π from a_2 to d_2 at the energy E_2.

Finally, we discuss the interplay of the two terms $N_1(E)$ and $N_2(E)$ in a finite concentration alloy. In the case of CuNi, Fig. 16 shows that $N_1(E)$ *decreases* in between the centers E_d^{Cu} and E_d^{Ni} of the Cu and Ni d resonances, and therefore, if taken alone would lead to a negative density of states in this region. The term $N_2(E)$ oscillates in just the opposite way and when added to $N_1(E)$ gives a final $N(E)$ curve which is monotonically increasing.[16]

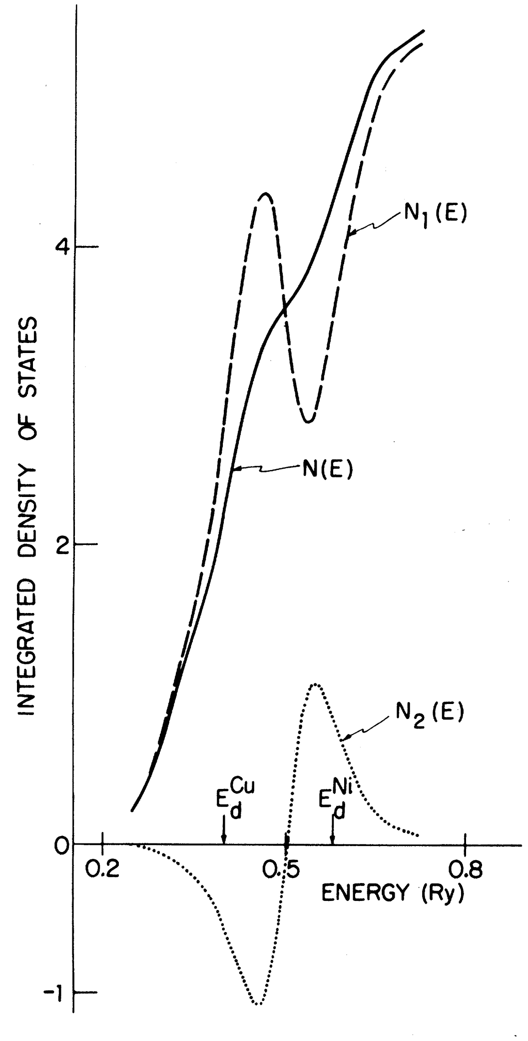

FIG. 16. Energy dependence of the terms $N_1(E)$ (dashed) (Ref. 59) $N_2(E)$ (dotted), and $N(E) = N_1(E) + N_2(E)$ [cf. Eq. (A4b)], in $\text{Cu}_{0.7}\text{Ni}_{0.3}$. See caption to Table I for definition of $E_d^{\text{Cu(Ni)}}$.

[*] Supported in part by Grant No. DMR 72-03209 A01 of the National Science Foundation.

[†] Supported in part by Grant Nos. DMR 72-02977 A03 and DMR 720 3020 of the National Science Foundation.

[1] M. Lax, Rev. Mod. Phys. 23, 287 (1951).

[2] R. J. Elliot, J. A. Krumhansl, and P. L. Leath, Rev. Mod. Phys. 46, 465 (1974).

[3] H. Ehrenreich and L. Schwartz, in *Solid State Physics*, edited by H. Ehrenreich, F. Seitz, and D. Turnbull (Academic, New York, to be published).

[4] P. Soven, Phys. Rev. 156, 809 (1967).

[5] B. Velický, S. Kirkpatrick, and H. Ehrenreich, Phys. Rev. 175, 747 (1968).

[6] J. Korringa, J. Phys. Chem. Solids 7, 252 (1958).

[7] J. L. Beeby, Proc. Roy. Soc. A302, 113 (1967).

[8] S. Kirkpatrick, B. Velický, and H. Ehrenreich, Phys. Rev. B 1, 3250 (1970).

[9] G. M. Stocks, R. W. Williams, and J. S. Faulkner, Phys. Rev. B 4, 4390 (1971).

[10] K. Levin and H. Ehrenreich, Phys. Rev. B 3, 4172 (1971).

[11] C. D. Gelatt, Jr. and H. Ehrenreich, Phys. Rev. B 10, 398 (1974).

[12] See Chap. 9 of Ref. 3 for a discussion of the muffin-tin alloy.

[13] A. Bansil, H. Ehrenreich, L. Schwartz, and R. E. Watson, Phys. Rev. B 9, 445 (1974).

[14] A. Bansil, L. Schwartz, and H. Ehrenreich, Phys. Kond. Mater. (to be published).

[15] L. Schwartz and A. Bansil, Phys. Rev. B 10, 3261 (1974).

[16] B. L. Gyorffy and G. M. Stocks, J. Phys. (Paris), 35, C4-75 (1974).

[17] P. Soven, Phys. Rev. B 2, 4715 (1970).

[18] For KKR method, see B. Segall and F. S. Ham, *Methods in Computational Physics*, edited by B. Alder, S. Fernbach, and M. Rotenberg (Academic, New York, 1968), Vol. 8; for APW method, see J. O. Dimmock, in *Solid State Physics*, edited by H. Ehrenreich, F. Seitz and D. Turbull (Academic, New York, 1971), Vol. 26.

[19] Preliminary results for disordered CuNi alloys were presented in A. Bansil, Ph.D. thesis (Harvard University, 1974) (unpublished).

[20] A. Bansil, Solid State Commun. 16, 885 (1975).

[21] W. Gudat and C. Kunz, Phys. Status Solidi 52, 433 (1972); A. Wenger, G. Burri, and S. Steinemann, Phys. Lett. A 34, 195 (1971); J. C. Love, F. E. Obenshain, and G. Czjzek, Phys. Rev. B 3, 2827 (1971).

[22] L. Hodges, R. E. Watson, and H. Ehrenreich, Phys. Rev. B 5, 3953 (1972).

[23] J. Friedel, Can. J. Phys. 34, 1190 (1956). P. W. Anderson, Phys. Rev. 124, 41 (1961).

[24] D. H. Seib and W. E. Spicer, Phys. Rev. B 2, 1676 (1970); 2, 1694 (1970).

[25] S. Hüfner, G. K. Wertheim, and J. H. Wernick, Phys. Rev. B 8, 4511 (1973).

[26] D. E. Eastman and W. F. Krolikowski, Phys. Rev. Lett. 21, 623 (1968).

[27] W. Krolikowski and W. E. Spicer, Phys. Rev. 185, 882 (1969).

[28] H. D. Drew and R. E. Doezema, Phys. Rev. Lett. 28, 1581 (1972).

[29] P. T. Coleridge and I. M. Templeton, Can. J. Phys. 49, 2449 (1971).

[30] D. L. Randles and M. Springford, Phys. Kond. Mater. (to be published).

[31] L. J. Rouse and P. G. Varlashkin, Phys. Rev. B 4, 2377 (1971).

[32] N. F. Mott, Adv. Phys. 13, 325 (1964).

[33] L. Huisman and J. Weiss, Solid State Commun. 16, 983 (1975).

[34] C. D. Gelatt, Jr., J. Weiss, and H. Ehrenreich (unpublished).

[35] The present discussion of the formalism is minimal. For details see Ref. 15.

[36] For example, H. Amar, K. H. Johnson, and C. B. Sommers, Phys. Rev. 153, 655 (1967); H. Amar, K. H. Johnson, and K. P. Wang, *ibid.* 148, 672 (1966).

[37] J. W. D. Connolly, Phys. Rev. 159, 415 (1967).

[38] N. D. Lang and H. Ehrenreich, Phys. Rev. 168, 605 (1968).

[39] The lattice constant of Cu decreases by approximately 0.025% per at.% Ni in Cu$_x$Ni$_{1-x}$, and increases by approximately 0.06% per at.% Zn in α-Cu$_x$Zn$_{1-x}$. [See W. B. Pearson, *A Handbook of Lattice Spacings and Structures of Metals and Alloys* (Pergamon, New York, 1958).]

[40] The results are based on the potential V_I^{Cu} unless noted otherwise.

[41] It should be emphasized that $a(\vec{k},E)$ is not the conventional spectral density $A(\vec{k},E) \equiv -(1/\pi)\,\mathrm{Im}\,\langle\vec{k}\,|\,G(E)\,|\,\vec{k}\rangle$. The quantity $\mathrm{Im}\,\langle\vec{k}\,|\,G(E)\,|\,\vec{k}\rangle$ cannot be expressed in terms of just the on-shell matrix elements $\tau_l^A(E)$ and $\tau_l^B(E)$.

[42] The calculations of Ref. 9 employ the CPA on a single-band model Hamiltonian, whereas we use ATA on a muffin-tin alloy. It is possible that the larger smoothing of the alloy spectrum (cf. Fig. 4) presented in Ref. 9 is, in part, due to the use of the CPA.

[43] D. E. Eastman, Phys. Rev. Lett. 26, 1108 (1971).

[44] C. N. Berglund, W. E. Spicer, Phys. Rev. A 136, 1030 (1964); 136, 1044 (1964).

[45] It should be emphasized that in pure metals, there is still controversy regarding the use of the "nondirect" transition model (Ref. 46). In particular, the fact that the peaks in photoemission profiles are found to vary as a function of the initial-state energy casts doubt on the validity of this assumption (Refs. 47 and 48). The application of this model to disordered alloys, although more reasonable, is also questionable.

[46] A. R. Williams, J. F. Janak and V. L. Moruzzi, Phys. Rev. Lett. 28, 671 (1972); V. L. Morruzi, A. R. Williams, and J. F. Janak, Phys. Rev. B 8, 2546 (1973).

[47] N. V. Smith, Phys. Rev. B 3, 1862 (1971).

[48] C. S. Fadley and D. A. Shirley, in *Electronic Density of States*, edited by L. H. Bennett, Natl. Bur. Stds. Spec. Publ. No. 323 (U. S. GPO, Washington, D. C., 1971).

[49] Ni and Ni-rich alloys are, of course, ferromagnetic. However, the size of the exchange splitting in CuNi (on the order of 0.5 eV) (Ref. 50) is small compared to either the constituent bandwidths (~4 eV) or the relative separations of the two d resonances (~2 eV). In addition, the photoemission studies of Pierce and Spicer (Ref. 51) show that the ferromagnetic splitting in CuNi alloys has an essentially negligible influence on the density of states. It seems reasonable, therefore, to neglect the effects of ferromagnetism in the present comparison of the gross features of the theory with experiment, as was done in Ref. 9.

[50] E. I. Zornberg, Phys. Rev. B 1, 244 (1970).

[51] D. T. Pierce and W. E. Spicer, Phys. Rev. Lett. 25,

[52] R. Haydock, V. Heine, M. J. Kelly, and J. B. Pendry, Phys. Rev. Lett. 29, 868 (1972).

[53] Clearly there exist reasonable estimates for $\Delta_d^{(r)}$ and $\Delta_d^{(i)}$ other than those given by (4.1) and (4.2). The differences between them, however, are small and are unimportant in the present context. For impurity concentrations approaching zero, $\Delta_d^{(r)} \ll \Delta_d^{(i)}$. In this limit, it is better to take $\Delta_d^{(i)}$ equal to the average damping in the Ni subband, because the VBS width results entirely from the broadening of the impurity states.

[54] The curves in Figs. 13 and 14 are based on the potential $V_{\mathrm{I}}^{\mathrm{Cu}}$. The use of $V_{\mathrm{II}}^{\mathrm{Cu}}$ would yield results identical to within 0.1 eV.

[55] C. L. Foiles, Phys. Rev. 169, 471 (1968).

[56] A. P. Klein and A. J. Heeger, Phys. Rev. 144, 458 (1966).

[57] S. Berko and J. Mader, Phys. Kond. Mater. (to be published).

[58] By contrast, in CuZn and CuH, the anisotropy of the Fermi-surface damping is more affected by differences in the s-p potentials of the two constituents. This point is discussed in Ref. 14.

[59] The subtraction of the free-electron singularities in the phase $N_1(\vec{k}, E)$ is assumed.